Iranian Journal of Geophysics, 2019, Page 33 - 49

New Improvement in Interpretation of Gravity Gradient Tensor Data Using Eigenvalues and Invariants: An Application to Blatchford Lake, Northern Canada

Mohammad Barazesh[1*]

[1]*M. Sc., Institute of Geophysics, University of Tehran, Tehran, Iran*

(Received: 10 September 2018, Accepted: 19 March 2019)

Abstract

Recently, interpretation of causative sources using components of the gravity gradient tensor (GGT) has had a rapid progress. Assuming N as the structural index, components of the gravity vector and gravity gradient tensor have a homogeneity degree of -N and - (N+1), respectively. In this paper, it is shown that the eigenvalues, the first and the second rotational invariants of the GGT (I1 and I2) are homogeneous with the homogeneity degree of - (N+1), -2(N+1) and -3(N+1), respectively. Furthermore, the product of M homogeneous functions with a homogeneity degree of - (N+1) itself is homogeneous with the degree of –M(N+1), and their summation do not change the homogeneity degree. Therefore, the Euler deconvolution of these functions can be used to estimate the location and type of the source, simultaneously. The advantage of using Euler deconvolution of invariants compared to other methods that use invariants is that the only parameters involved in location approximation are invariants and their derivatives. Therefore, it is completely independent of the orientation of the coordinate system as well as having little sensitivity to random noise. In this study, the model is tested on synthetic models with and without noise. Finally, application of the method has been demonstrated on measured gravity gradient tensor data set from the Blatchford Lake area, Southeast of Yellowknife, Northern Canada.

Keywords: gravity gradient tensor, eigenvalues, rotational invariant

*Corresponding author: Barazeshm@ut.ac.ir

1 Introduction

GGT data have an important application in extracting more details from subsurface structures, especially in oil, mine and sulfide reservoir exploration. Many techniques have been designed, which use the components of gradient tensor and/or their derivatives to interpret gravity or magnetic anomaly sources (Mikhailov et al., 2007; Beiki, 2010; Oruç, 2010; Beiki et al., 2012; Beiki et al., 2014; Zhou, 2016). The GGT is defined in terms of the second-order spatial derivatives of gravitational potential as follows (Pedersen and Rasmussen, 1990):

$$\Gamma = \begin{pmatrix} \frac{\partial^2 U}{\partial x^2} & \frac{\partial^2 U}{\partial x \partial y} & \frac{\partial^2 U}{\partial x \partial z} \\ \frac{\partial^2 U}{\partial x \partial y} & \frac{\partial^2 U}{\partial y^2} & \frac{\partial^2 U}{\partial y \partial z} \\ \frac{\partial^2 U}{\partial x \partial z} & \frac{\partial^2 U}{\partial y \partial z} & \frac{\partial^2 U}{\partial z^2} \end{pmatrix} = \begin{pmatrix} g_{xx} & g_{xy} & g_{xz} \\ g_{xy} & g_{yy} & g_{yz} \\ g_{xz} & g_{yz} & g_{zz} \end{pmatrix} \quad (1)$$

where U is the gravitational potential. Due to the gravity field conservation and displacement of differential operators, the tensor components are real and symmetric, $Tr(\Gamma) = g_{xx} + g_{yy} + g_{zz} = 0$. Therefore in a free space, the gradient tensor only has five independent components.

The components of GGT are more sensitive to low wavelength anomalies compared to components of the gravity vector. The eigenvalues of GGT $\lambda_i \, (i = 1,2,3)$ could be calculated by solving the following characteristic equation (Pedersen and Rasmussen, 1990; Beiki et al., 2012):

$$\lambda^3 + I_1 \lambda - I_2 = 0 \quad (2)$$

where I_1 and I_2 are rotational invariants of GGT, which are not affected by coordination system rotation and any analytical function of them possesses this property as well. The components of GGT may be obtained via either calculation or direct measurement. To calculate the components of the gravity gradient tensor, the method introduced by Mickus and Hinojosa (2001) is used. Nevertheless, as the measured GGT data are now widely accessible with high quality, eigenvalues and other values such as rotational invariants could be directly calculated from the measured GGT data. Pederson and Rasmussen (1990) introduced scalar invariants in terms of GGT components, which can be used as a tool for enhancing anomalies due to their lateral resolution compared to the corresponding field.

These invariants could be written as:

$$\begin{aligned} I_1 &= g_{xx} g_{yy} + g_{yy} g_{zz} + g_{xx} g_{zz} \\ &\quad - g_{xy}^{\ 2} - g_{yz}^{\ 2} - g_{xz}^{\ 2} \\ &= \lambda_1 \lambda_2 + \lambda_2 \lambda_3 + \lambda_1 \lambda_3 \\ &= -\frac{\lambda_1^{\ 2} + \lambda_2^{\ 2} + \lambda_3^{\ 2}}{2} \end{aligned} \quad (3)$$

$$\begin{aligned} I_2 &= g_{xx} g_{yy} g_{zz} + 2 g_{xy} g_{yz} g_{xz} \\ &\quad - g_{yz}^{\ 2} g_{xx} - g_{xz}^{\ 2} g_{yy} - g_{xy}^{\ 2} g_{zz} \\ &= \lambda_1 \lambda_2 \lambda_3 \end{aligned} \quad (4)$$

where $\lambda_1 \geq \lambda_2 \geq \lambda_3$, and λ_2 has the lowest absolute value (Beiki et al., 2012).

For 2D structures $\lambda_2 = 0$ and $\lambda_1 = -\lambda_3$, therefore $I_1 = -\lambda_1^{\ 2} = -\lambda_3^{\ 2}$ and $I_2 = 0$. Nabighian (1984) introduced the 2D analytical signal and showed that Hilbert transforms of any potential field satisfy Cauchy-Riemann relationships. Roest et al. (1992) extended the analytical signal amplitudes of the potential field *f(x, y)* to 3D:

$$A(x,y) = \sqrt{\left[\frac{\partial f(x,y)}{\partial x}\right]^2 + \left[\frac{\partial f(x,y)}{\partial y}\right]^2 + \left[\frac{\partial f(x,y)}{\partial z}\right]^2} \quad (5)$$

By substituting each component of gravity vector ($\vec{g} = (g_x, g_y, g_z)$) in *f(x, y)*, the directional analytical signal could be

obtained in x, y and z directions as follows (Beiki, 2010):

$$A_x(x,y)=\sqrt{g_{xx}^{\ 2}+g_{xy}^{\ 2}+g_{xz}^{\ 2}} \tag{6}$$

$$A_y(x,y)=\sqrt{g_{xy}^{\ 2}+g_{yy}^{\ 2}+g_{yz}^{\ 2}} \tag{7}$$

$$A_z(x,y)=\sqrt{g_{xz}^{\ 2}+g_{yz}^{\ 2}+g_{zz}^{\ 2}} \tag{8}$$

Using the Laplacian equation ($g_{yy}+g_{zz}=-g_{xx}$) and some algebraic simplification, the first rotational invariant (I_1) can be obtained in terms of directional analytical signals as follows:

$$\begin{aligned} I_1 &= g_{xx}(g_{yy}+g_{zz}) \\ &\quad + \frac{(g_{yy}+g_{zz})^2 - g_{yy}^{\ 2} - g_{zz}^{\ 2}}{2} \\ &\quad - g_{xy}^{\ 2} - g_{yz}^{\ 2} - g_{xz}^{\ 2} \\ &= -\frac{g_{xx}^{\ 2}+g_{xy}^{\ 2}+g_{xz}^{\ 2}}{2} \\ &\quad - \frac{g_{xy}^{\ 2}+g_{yy}^{\ 2}+g_{yz}^{\ 2}}{2} \\ &\quad - \frac{g_{xz}^{\ 2}+g_{yz}^{\ 2}+g_{zz}^{\ 2}}{2} \\ &= -\frac{A_x^{\ 2}+A_y^{\ 2}+A_z^{\ 2}}{2} \end{aligned} \tag{9}$$

As could be seen from the above equation, this function always has a negative value.

Wilson (1985) introduced an important quantity called normalized source strength in terms of eigenvalues (Clark, 2012):

$$\mu=\sqrt{-\lambda_2^{\ 2}-\lambda_1\lambda_3}=\sqrt{-I_1-2\lambda_2^{\ 2}} \tag{10}$$

Beiki et al. (2012) showed that the normalized magnetic source strength is independent of source magnetization direction. They also proved that the normalized source strength satisfies Euler's equation and could be used to locate magnetic sources. Pilkington & Beiki (2013) presented an algorithm for illustration of source magnetic distribution using normalized source strength.

2 An overview to Euler deconvolution method

The $f(\mathbf{r})$ would be a homogenous function with the degree of n and each real parameter, t, when (Reid et al., 1990; Reid et al., 2014):

$$f(t\mathbf{r})=t^n f(\mathbf{r}) \tag{11}$$

where $\mathbf{r}=(x_1, x_2, \ldots, x_k)$ and n is a positive integer. The homogeneous functions satisfy Euler's differential equation. Therefore,

$$\mathbf{r}\,\nabla f(\mathbf{r})=n\,f(\mathbf{r}) \tag{12}$$

According to this definition, the magnetic and gravity fields resulted from a number of simple sources are homogenous functions in spatial coordinate. However, in practice, Euler's equation could be used for sources with arbitrary shapes.

Zhang et al. (2000) indicated that the horizontal components of gravitational vector in x, and y directions work as vertical component in homogeneous Euler's equation:

$$\begin{aligned} &(x-x_0)\frac{\partial g_x}{\partial x}+(y-y_0)\frac{\partial g_x}{\partial y} \\ &\quad +(z-z_0)\frac{\partial g_x}{\partial z}=N(B_x-g_x) \end{aligned} \tag{13}$$

$$\begin{aligned} &(x-x_0)\frac{\partial g_y}{\partial x}+(y-y_0)\frac{\partial g_y}{\partial y} \\ &\quad +(z-z_0)\frac{\partial gy}{\partial z}=N(B_y-g_y) \end{aligned} \tag{14}$$

$$\begin{aligned} &(x-x_0)\frac{\partial g_z}{\partial x}+(y-y_0)\frac{\partial g_z}{\partial y} \\ &\quad +(z-z_0)\frac{\partial g_z}{\partial z}=N(B_z-g_z) \end{aligned} \tag{15}$$

where N is the structural index and B_x, B_y and B_z are regional anomaly parameters of gravity vector components in the direction of x, y and z, which are assumed to be constant. $P(x,y,z)$ and $P_0\ (x_0,y_0,z_0)$ are the observed points and the source location, respectively. In the above equations, the structural index N should be determined by the user based on the previous

information. The structural index is given in Table 1 for some simple gravity sources. By differentiation of the Equation (13) in x, y and z,

$$(x-x_0)\frac{\partial g_{xx}}{\partial x}+(y-y_0)\frac{\partial g_{xx}}{\partial y}+(z-z_0)\frac{\partial g_{xx}}{\partial z}=-(N+1)g_{xx} \quad (16)$$

$$(x-x_0)\frac{\partial g_{yx}}{\partial x}+(y-y_0)\frac{\partial g_{yx}}{\partial y}+(z-z_0)\frac{\partial g_{yx}}{\partial z}=-(N+1)g_{yx} \quad (17)$$

$$(x-x_0)\frac{\partial g_{zx}}{\partial x}+(y-y_0)\frac{\partial g_{zx}}{\partial y}+(z-z_0)\frac{\partial g_{zx}}{\partial z}=-(N+1)g_{zx} \quad (18)$$

where $g_{\alpha\beta}=\frac{\partial g_\beta}{\partial \alpha}$ ($\alpha,\beta=x,y$ and z) are the components of GGT. These equations show that components g_{xx}, g_{yx} and g_{zx} are homogeneous with homogeneity degree of – (N+1) (according to Equation (11), (N+1) should be positive). Beiki (2010) demonstrated for some simple sources that the directional analytical signals are homogeneous and satisfy Euler's equation. It can be shown using Equations (13) to (15), and it is only proved for A_x. By multiplying the Equations (16), (17) and (18) to g_{xx}, g_{yx} and g_{zx} respectively, and adding all three equations,

$$\begin{aligned}&(x-x_0)(g_{xx}\frac{\partial g_{xx}}{\partial x}+g_{yx}\frac{\partial g_{yx}}{\partial x}+g_{zx}\frac{\partial g_{zx}}{\partial x})+\\&(y-y_0)(g_{xx}\frac{\partial g_{xx}}{\partial y}+g_{yx}\frac{\partial g_{yx}}{\partial y}+g_{zx}\frac{\partial g_{zx}}{\partial y})+\\&(z-z_0)(g_{xx}\frac{\partial g_{xx}}{\partial z}+g_{yx}\frac{\partial g_{yx}}{\partial z}+g_{zx}\frac{\partial g_{zx}}{\partial z})\\&=-(N+1)(g_{xx}{}^2+g_{yx}{}^2+g_{zx}{}^2)\\&=-(N+1)A_x{}^2\end{aligned} \quad (19)$$

And with dividing above equation by A_x,

$$(x-x_0)\frac{\partial A_x}{\partial x}+(y-y_0)\frac{\partial A_x}{\partial y}+(z-z_0)\frac{\partial A_x}{\partial z}=-(N+1)A_x \quad (20)$$

where,

$$\frac{\partial A_x}{\partial \alpha}=\frac{1}{A_x}(g_{xx}\frac{\partial g_{xx}}{\partial \alpha}+g_{yx}\frac{\partial g_{yx}}{\partial \alpha}+g_{zx}\frac{\partial g_{zx}}{\partial \alpha})$$

and $\alpha=x,y,z$.

Through performing these steps for Equation (14) and (15), a similar expression to Equation (20) can be obtained for A_y and A_z,

$$(x-x_0)\frac{\partial A_y}{\partial x}+(y-y_0)\frac{\partial A_y}{\partial y}+(z-z_0)\frac{\partial A_y}{\partial z}=-(N+1)A_y \quad (21)$$

$$(x-x_0)\frac{\partial A_z}{\partial x}+(y-y_0)\frac{\partial A_z}{\partial y}+(z-z_0)\frac{\partial A_z}{\partial z}=-(N+1)A_z \quad (22)$$

The above equations prove that the directional analytical signal in x, y and z is homogeneous with a homogeneity degree of – (N+1). The derivatives of directional analytical signal in x, y and z directions could be obtained in terms of GGT components and its derivatives (Beiki, 2010). Therefore, with omitting the constant parameters, B, one can simultaneously calculate location and structural index using Euler's equation.

This paper showed that the eigenvalues and rotational invariants of GGT are homogeneous and satisfied Euler's equation. While the components of GGT change due to their projection onto the base coordinate axis, the invariants are completely independent of the orientation of the coordinate system. Due to simultaneous use of all components of GGT, these quantities are less susceptible to random noise and better preserve the size and shape of the sources. Therefore, it is an effective way to estimate the location

and type of the gravity anomaly sources.

3 The homogeneity of gravity gradient tensor eigenvalues and invariants

Below, the homogeneity of directional analytical signal is used to prove that the first invariant (I_1) of GGT is homogeneous. By multiplying Equations (19), (20) and (21) to A_x, A_y and A_z respectively, and collecting them,

$$\begin{aligned}&(x-x_0)(\frac{\partial A_x}{\partial x}A_x+\frac{\partial A_y}{\partial x}A_y+\frac{\partial A_z}{\partial x}A_z)+\\&(y-y_0)(\frac{\partial A_x}{\partial y}A_x+\frac{\partial A_y}{\partial y}A_y+\frac{\partial A_z}{\partial y}A_z)+\\&(z-z_0)(\frac{\partial A_x}{\partial z}A_x+\frac{\partial A_y}{\partial z}A_y+\frac{\partial A_z}{\partial z}A_z)=\\&\qquad -(N+1)(A_x^{\,2}+A_y^{\,2}+A_z^{\,2})\end{aligned} \tag{23}$$

Therefore, according to Equation (9), it is obtained

$$\begin{aligned}&(x-x_0)\frac{\partial I_1}{\partial x}+(y-y_0)\frac{\partial I_1}{\partial y}\\&\quad+(z-z_0)\frac{\partial I_1}{\partial z}=-2(N+1)I_1\end{aligned} \tag{24}$$

Thus, the homogeneity degree of I_1 is twice the homogeneity degree of directional analytical signals. The Equation (24) can be written in matrix form for a window with m points as below:

$$\begin{pmatrix}(\frac{\partial I_1}{\partial x})_1 & (\frac{\partial I_1}{\partial y})_1 & (\frac{\partial I_1}{\partial z})_1 & 2(I_1)_1\\ \vdots & \ddots & & \vdots\\ \vdots & & \ddots & \vdots\\ (\frac{\partial I_1}{\partial x})_m & (\frac{\partial I_1}{\partial y})_m & (\frac{\partial I_1}{\partial z})_m & 2(I_1)_m\end{pmatrix}\begin{pmatrix}x_0\\y_0\\z_0\\-N\end{pmatrix}= \tag{25}$$

$$\begin{pmatrix}x_1(\frac{\partial I_1}{\partial x})_1+y_1(\frac{\partial I_1}{\partial y})_1+z_1(\frac{\partial I_1}{\partial z})_1+2(I_1)_1\\ \vdots\\ \vdots\\ x_m(\frac{\partial I_1}{\partial x})_m+y_m(\frac{\partial I_1}{\partial y})_m+z_m(\frac{\partial I_1}{\partial z})_m+2(I_1)_m\end{pmatrix}$$

Table 1. Structural index (N) for different gravity sources (after Phillips et al., 2007).

Gravity source	Structural index (N)
Point source (Sphere)	2
Horizontal cylinder	1
Thin sheet edge	0
Contact	-1

The derivatives of the I_1 in terms of the derivatives of the directional analytical signal are:

$$\frac{\partial I_1}{\partial \alpha}=-(\frac{\partial A_x}{\partial \alpha}A_x+\frac{\partial A_y}{\partial \alpha}A_y+\frac{\partial A_z}{\partial \alpha}A_z) \tag{26}$$

where $\alpha=x,y,z$.

According to the Equation (3) and homogeneity of the first rotational invariant (I_1), one can see that the expression $\lambda_1^{\,2}+\lambda_2^{\,2}+\lambda_3^{\,2}$ is homogeneous as well. It is simple to prove the homogeneity of eigenvalues for a number of simple sources by applying relationships of Pederson and Rasmussen (1990). In the following, this will be demonstrated for the second eigenvalue (λ_2) from homogeneity of invariant I_1. Beiki et al. (2014) expanded normalized source strength (μ) to gravity ones and showed that $\mu \propto 1/r^{N+1}$. Therefore, it is homogeneous function with the homogeneity degree of - (N + 1) and satisfies the Euler's equation. Therefore, due to homogeneity of I_1 and μ, and using the Equation (10),

$$\begin{aligned}&\lambda_2(\mu,I_1)=(-\frac{1}{2}(\mu^2+I_1))^{\frac{1}{2}}\Rightarrow\\&\lambda_2'=\lambda_2(t\mu,tI_1)=(-\frac{1}{2}(\mu'^2+I_1'))^{\frac{1}{2}}\\&\quad=(-\frac{1}{2}((t^{-(N+1)}\mu)^2+t^{-2(N+1)}I_1))^{\frac{1}{2}}\\&\quad=t^{-(N+1)}\lambda_2\end{aligned} \tag{27}$$

It means that λ_2 is homogeneous with the homogeneity degree of – (N+1). In addition, this could be proved for other eigenvalues. Therefore, the eigenvalues of GGT satisfy the Euler's equation:

$$(x-x_0)\frac{\partial\lambda_1}{\partial x}+(y-y_0)\frac{\partial\lambda_1}{\partial y}+(z-z_0)\frac{\partial\lambda_1}{\partial z}=-(N+1)\lambda_1 \quad (28)$$

$$(x-x_0)\frac{\partial\lambda_2}{\partial x}+(y-y_0)\frac{\partial\lambda_2}{\partial y}+(z-z_0)\frac{\partial\lambda_2}{\partial z}=-(N+1)\lambda_2 \quad (29)$$

$$(x-x_0)\frac{\partial\lambda_3}{\partial x}+(y-y_0)\frac{\partial\lambda_3}{\partial y}+(z-z_0)\frac{\partial\lambda_3}{\partial z}=-(N+1)\lambda_3 \quad (30)$$

For the 2D sources, Equation (29) equals to zero, and Equation (28) and (30) give the same results. The directional derivatives of eigenvalues could be calculated in terms of invariants derivatives or GGT derivatives (Clark, 2012; Beiki et al., 2012). Using Equation (28) to (30) it could be shown that the second invariant (I_2) is also homogeneous,

$$(x-x_0)\frac{\partial\lambda_1}{\partial x}\lambda_2\lambda_3+(y-y_0)\frac{\partial\lambda_1}{\partial y}\lambda_2\lambda_3+(z-z_0)\frac{\partial\lambda_1}{\partial z}\lambda_2\lambda_3=-(N+1)\lambda_1\lambda_2\lambda_3 \quad (31)$$

$$(x-x_0)\frac{\partial\lambda_2}{\partial x}\lambda_1\lambda_3+(y-y_0)\frac{\partial\lambda_2}{\partial y}\lambda_1\lambda_3+(z-z_0)\frac{\partial\lambda_2}{\partial z}\lambda_1\lambda_3=-(N+1)\lambda_1\lambda_2\lambda_3 \quad (32)$$

$$(x-x_0)\frac{\partial\lambda_3}{\partial x}\lambda_1\lambda_2+(y-y_0)\frac{\partial\lambda_3}{\partial y}\lambda_1\lambda_2+(z-z_0)\frac{\partial\lambda_3}{\partial z}\lambda_1\lambda_2=-(N+1)\lambda_1\lambda_2\lambda_3 \quad (33)$$

Therefore, by summation of the Equations (31) to (33),

$$(x-x_0)\frac{\partial I_2}{\partial x}+(y-y_0)\frac{\partial I_2}{\partial y}+(z-z_0)\frac{\partial I_2}{\partial z}=-3(N+1)I_2 \quad (34)$$

The derivatives of *I2* could be calculated in three Cartesian directions x, y and z using derivatives of the expression introduced by Pedersen and Rasmussen (1990) for canonical invariants in terms of GGT components. The derivatives of I_2 in terms of eigenvalues is as follows:

$$\frac{\partial I_2}{\partial\alpha}=\frac{\partial\lambda_1}{\partial\alpha}\lambda_2\lambda_3+\frac{\partial\lambda_2}{\partial\alpha}\lambda_1\lambda_3+\frac{\partial\lambda_3}{\partial\alpha}\lambda_1\lambda_2 \quad (35)$$

where $\alpha=x,y,z$.

Efficiency of the above equation loses for 2D sources, which $I_2=0$.

Pedersen and Rasmussen (1990) introduced the invariant ratio, I (Equation (A1) at appendix A), which is defined as the ratio of two invariants (I_1 and I_2). This quantity indicates that the causative source is two-dimensional or three-dimensional. Furthermore, it is shown in Appendix A that invariant ratio (I) is homogeneous with zero homogeneity degree and satisfied Euler's equation.

To apply the Euler's deconvolution method, an algorithm presented by Beiki et al. (2012) was used. According to their algorithm, a square window is formed with initial size, centered with the maxima of homogeneous function or its vertical derivative. Then, the data of this window was used to estimate the location of source and the structural index. The size of the window was increased to a specific user-defined range.

Then, among the set of solutions for different window size, a solution with the lowest uncertainty normalized to estimated parameters was selected as the location and structural index of the source. The uncertainty in the location and the structural index of the source could be calculated from the covariance matrix as described by Beiki (2010). An advantage of this algorithm is the reduction of computation time as well as choosing points with higher signal within the window.

4 Application to the synthetic model

The efficiency of the described method is tested on a prism with dimensions 300×300×300 m^3, the top depth of 20 meters and density contrast 1 gr/cm^3. Figure 1a shows the λ_1 map for this model.

It could be seen that the maximum of this eigenvalue is slightly shifted inward from edges of the prism. To apply Euler's deconvolution method, the algorithm introduced by Beiki et al. (2012) was used. In this algorithm, the absolute value of the function or its vertical derivative is used for depth estimation in Euler's equation. This study rejected the negative depths and unreasonable structural index (outside of -1≤N≤2) from Euler's solutions. For this model, a window of 15 m×15 m was used centered on the maximum of $\frac{\partial \lambda_1}{\partial z}$. Afterwards, the length of the window was increased as far as both of the edges reached to 160 m. Finally, the solution was selected with the least uncertainty normalized to calculated parameters in estimation of location or structural index (also, the negative depths and unreasonable structural index is rejected). Figure 1b shows the results of depth estimation for λ_1 function, which are traced with black dots on this function map. Figures 1c and 1d show histograms of depth and structural index, respectively. The calculated depth is very close to the top depth of prism, and the negative structural index is obtained. It shows that solutions over the edges are corresponding to the contact model. The estimated results cover the edges and corners very well. Similar to the λ_1, the results of depth and structural index estimation via Euler's deconvolution of λ_2, I_1 and I_2 are illustrated in Figures 2 to 4, respectively. According to Figure 2, the estimations of the second eigenvalue

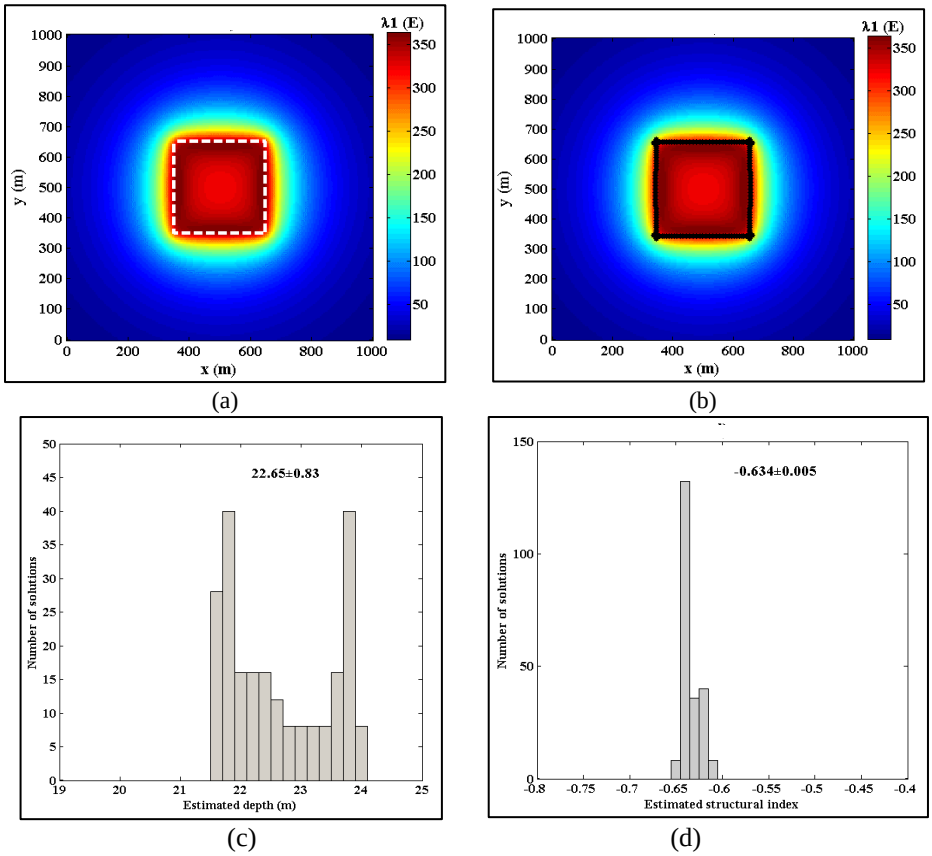

Figure 1. (a) λ_1 map corresponding to a prism with dimensions of 300×300×300 m^3 and depth to top of 20 m. Dashed line is outline of prism. (b) Solutions of Euler deconvolution of λ_1 (black circles) for the prism shown in (a). (c) Histogram of estimated depth and (d) histogram of structural index of the prism.

are located on the corners toward the center of the prism, and the results are very close to the correct values as well as the first eigenvalue. In this case, $|\lambda_2|$ was used to extract the maximum.

The results of the first rotational invariant (Figure 3) show a higher continuity. This function always returns a negative value and is minimized on the edges. Therefore, I used $\left|\frac{\partial I_1}{\partial z}\right|$ to extract the maximum. The second rotational invariant (I_2), which is the product of three eigenvalues of GGT, is usually maximized on the edges. $\frac{\partial I_2}{\partial z}$ was used to determine the maximum. The results of horizontal location for this function are exactly coincided on the center of edges and corners (Figure 4). The results of depth and structural index for each of these functions are very close to each other.

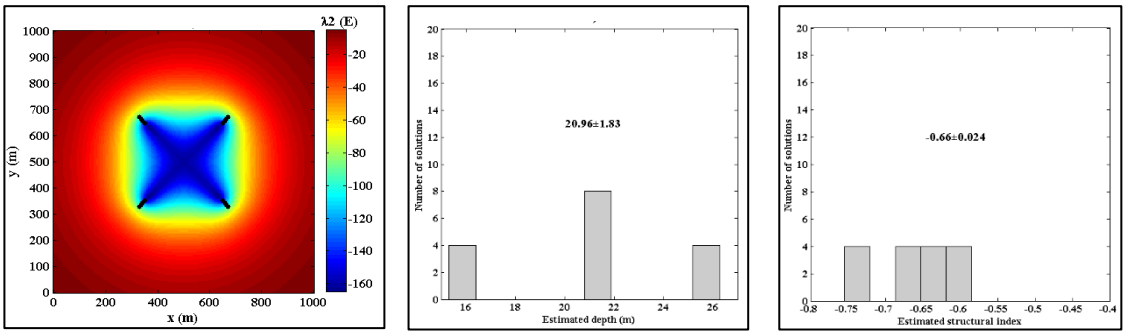

(a) (b) (c)

Figure 2. (a) λ_2 map superimposed by solutions of Euler deconvolution (black circles). (b) Histogram of estimated depth and (c) histogram of structural index of the prism.

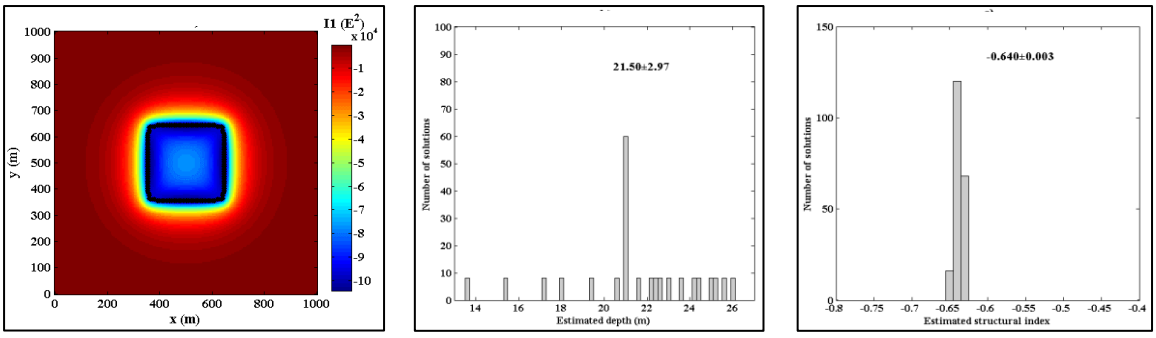

(a) (b) (c)

Figure 3. (a) I_1 map superimposed by solutions of Euler deconvolution (black circles). (b) Histogram of estimated depth and (c) histogram of structural index of the prism.

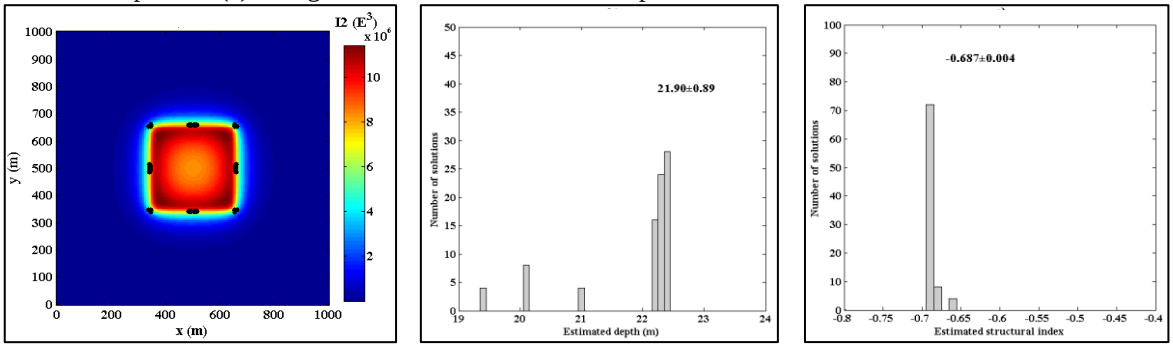

(a) (b) (c)

Figure 4. (a) I_2 map superimposed by solutions of Euler deconvolution (black circles). (b) Histogram of estimated depth and (c) histogram of structural index of the prism.

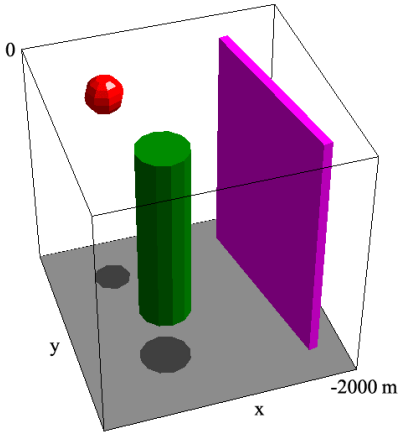

Figure 5. 3D view of a synthetic model.

5 The effect of interfering sources

To study the sensitivity of the method to the interference, the model shown in Figure 5 is used. This model consists of three bodies with different density contrasts and depths. The physical and geometrical properties are presented in Table 2. The Gaussian noise $N(0, \sigma^2)$ with a standard deviation of 1 Eötvös (10% of the standard deviation of g_{zz}) was added to each of GGT components. Then, the eigenvalues and rotational invariants were calculated from these components. Figure 6a shows the g_{zz} component for this model. The Figures 6b and 6c show the I_1 and I_2, respectively. As shown in these figures, maxima of these functions are distorted with noise. Therefore, applying a filter to reduce the noise effect is essential. To reduce the effect of noise and prevent the selection of invalid maxima, upward continuation of 20 m was applied to GGT components before applying Euler's equation. The eigenvalues and rotational invariants were calculated from upward continued gradient tensor components. Figure 6d shows I_2 after upward continuation of 20 m. As can be seen in this figure, the maxima determined the source location correctly. For any Euler's equation, a square window with a size of 15 m×15 m was selected as the starting window. Then, the window size was

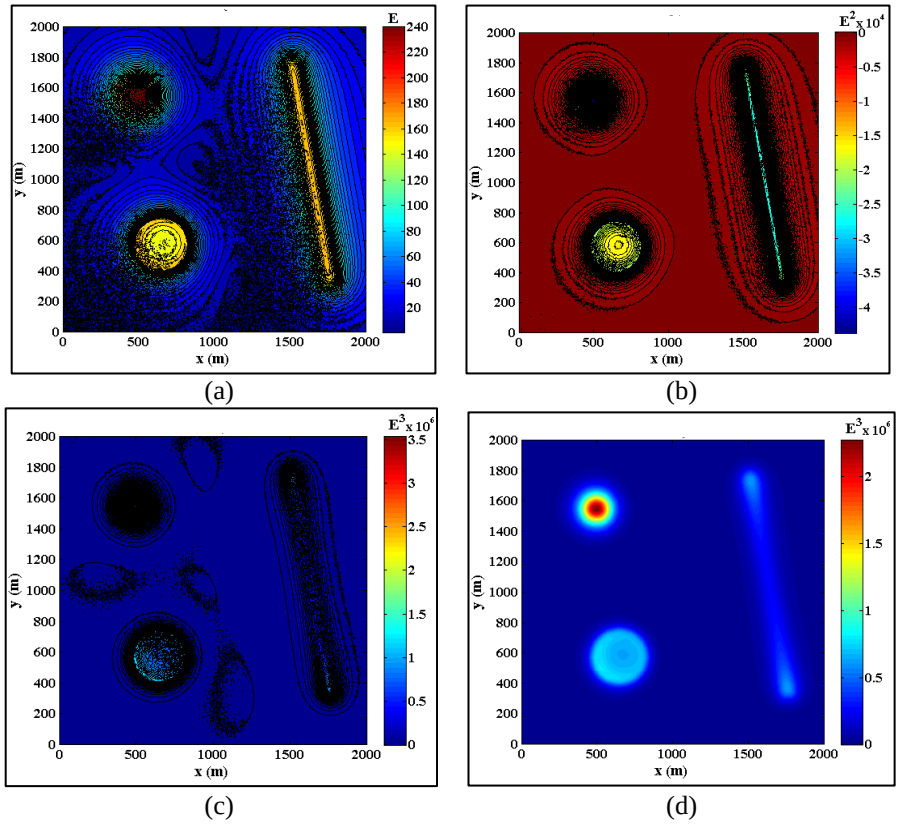

Figure 6. (a) g_{zz} of the model shown in Figure 5 in presence of Gaussian random noise with zero mean and standard deviation of 1E. (b) I_1 and (c) I_2 map of the model in presence of noise. (d) Invariant I_2 after upward continuation of 20 m.

Table 2. Physical and geometrical properties of bodies shown in Figure 5.

Body	Depth to top/ center (m)	Depth extent (m)	Strike length (m)	Thickness/ Radius (m)	Density contrast (g/cm^3)
Sphere	200	-	-	150	1.3
Prism	50	2000	1500	75	1.25
Pipe	20	1500	-	200	1.1

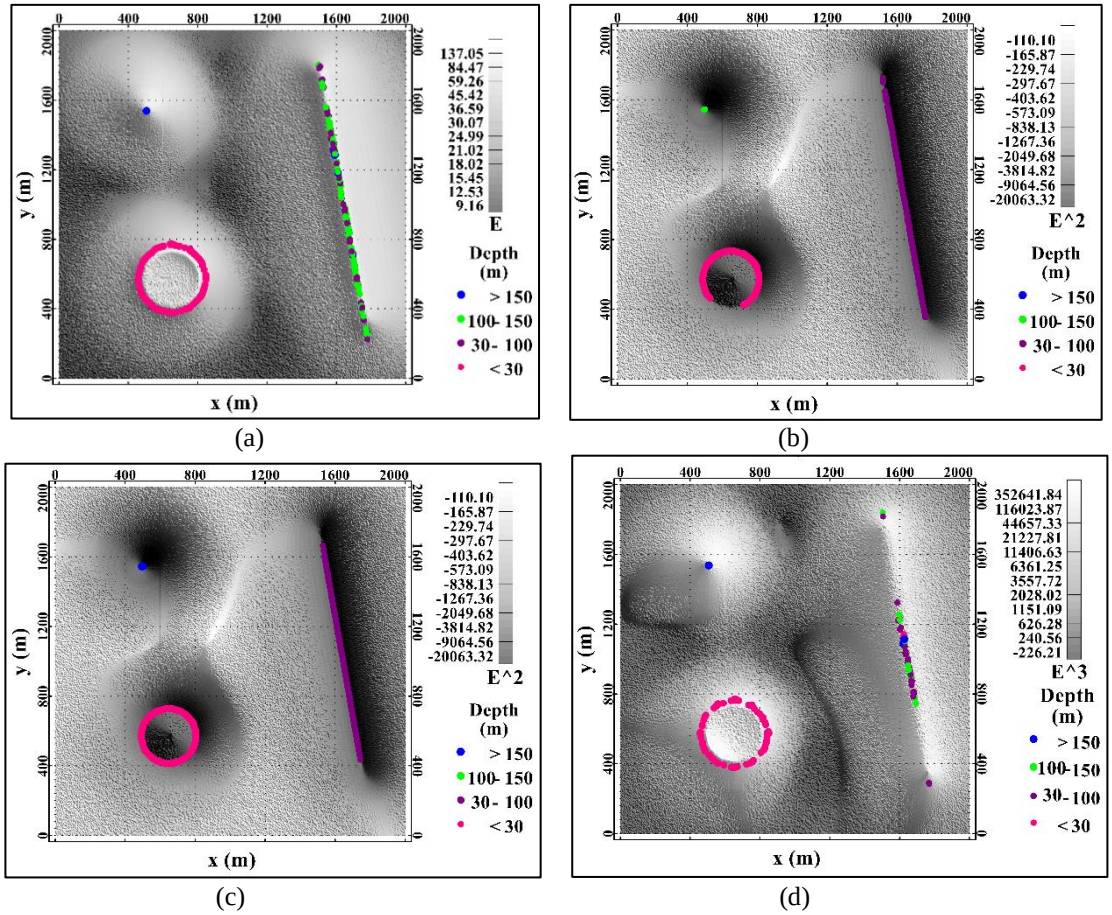

Figure 7. The estimated depths of the model shown in Figure 5 from Euler deconvolution of (a) λ_1, (b) three eigenvalues (λ_1, λ_2 and λ_3), (c) I_1 and (d) I_2 after upward continuation of 20 m.

increased to the threshold size 100 m×100 m. The estimated source locations and structural indices for each function superimposed on corresponding maps in Figures 7 and 8, respectively.

Figures 7a and 7b show the results of depth estimation for the λ_1 and considering three eigenvalues, respectively. As could be seen from these figures, the estimations of pipe exactly fall on its curve edges whereas in Figure 7b the estimations are slightly shifted inward. For Figure 7b, the maxima of $\frac{\partial \lambda_1}{\partial z}$ was used in calculations. Figures 7c and 7d show depth estimations for I_1 and I_2. As could be seen in Figure 6d, the 2D state gets closer to the 3D state by approaching to corners of prism. As a result, the signal starts to increase from zero. Therefore, this function has lower estimates in the center of prism. Figure 8 shows the estimated structural index corresponding to Figure 7. The results shown in Figures 7 and 8 are valid estimations of location and type of the source.

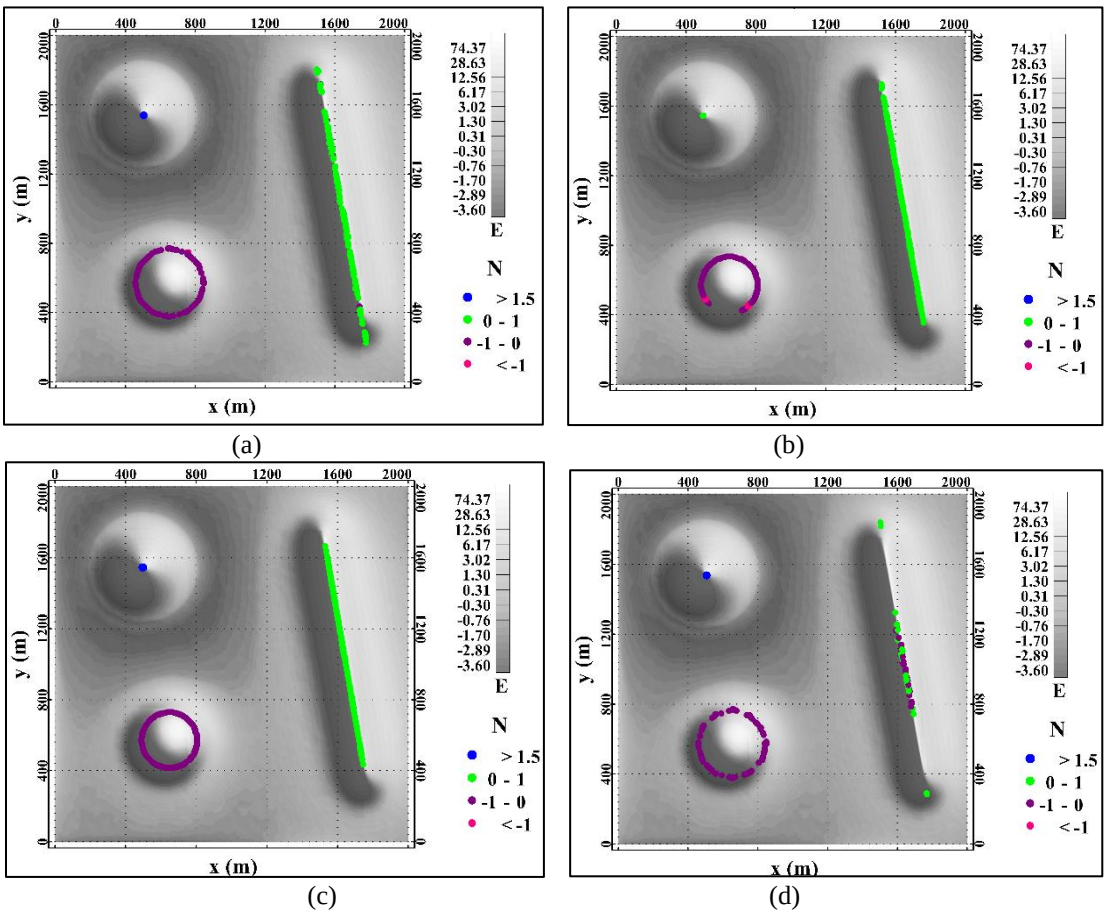

Figure 8. The estimated structural index of the model shown in Figure 5 from Euler deconvolution of (a) λ_1, (b) tree eigenvalues (λ_1, λ_2 and λ_3), (c) I_1 and (d) I_2 after upward continuation of 20 m.

To examine the deviation of the estimated parameters from the true values in the presence of interfering sources, two spheres are considered, the centers of which are separated by S. The spheres are at a depth of 100 meters, a radius of 50 meters and a density contrast of 1gr/cm^3. Figure 9a shows the computed analytic signal (*AS*), $\left|\frac{\partial I_1}{\partial z}\right|$ and $\frac{\partial I_2}{\partial z}$ for S = Z. Each of these functions is normalized to its maximum values. As you can see from this figure, the function $\frac{\partial I_2}{\partial z}$ has a higher resolution than two other functions.

Figure 9b shows the relative error of the calculated depth and structural index from true values, $\frac{\left|m^{est}-m^{tru}\right|}{m^{tru}}\times 100$ for different values of S/Z (separation-to-depth ratio) that m^{est} and m^{tru} represent the estimated and correct parameters, respectively. When S=0, the estimated values are close to true ones because in this situation, the two spheres are indistinguishable and appear as a sphere with a density contrast of 2gr/cm^3. By increasing *S/Z*, the relative error also increases, and at S = Z it reaches to its maximum error. For *S*> *Z*, the error decreases and the calculated parameters go to true values. It should be noted that for this model, the error generated by the function I_2 is lower than I_1.

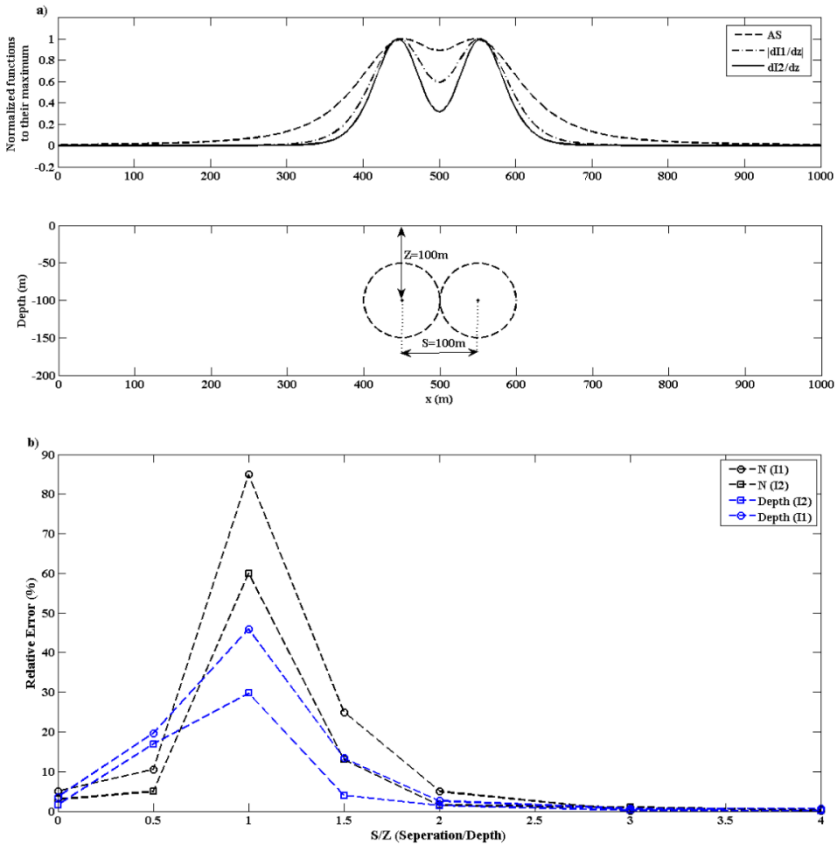

Figure 9. (a) *AS*, $\left|\frac{\partial I_1}{\partial z}\right|$ and $\frac{\partial I_2}{\partial z}$ for two spheres located at depth Z (=100 m) and separation of S (=100), (b) relative error of the calculated depth (dashed blue lines) and structural index (N) (dashed black lines) from true values plotted versus different separation to depth (S/Z).

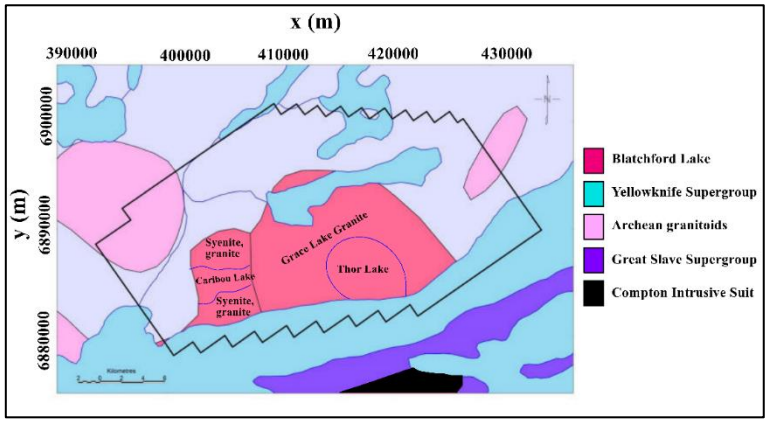

Figure 10. Simplified regional geology setting of the Blatchford Lake area modified from Geological survey of Canada (2011).

6 Blatchford Lake area

The Blatchford Lake area is located in central Northwest Territories approximately 80 km southeast of Yellowknife (Figure 10). Birkett et al. (1994) show 3D modelling of the Blatchford Lake area, including syenite, both metaluminous and peralkaline granites, and the associated Thor Lake rare-metal deposits. Their studies showed that the Blatchford Lake area is a relatively thin body with tabular geometry.

Davidson (1978, 1981 and 1982) has shown that the Blatchford Lake area divisible into two parts; the western lobe and the eastern lobe. The western lobe rocks include mafic intrusive rocks of the Caribou Lake Gabbro (an area of approximately 20 km^2), syenites and granites.

The composition of these rocks vary from olivine-gabbro-neritic to plagioclase-rich leucoferrodiorite from western contacts toward eastern contacts.

Northwest- and east-northeast trending diabase dykes cut all geological units in the western lobe. The eastern lobe rocks, which are laterally more extensive and geometrically subcircular, consist mainly of Grace Lake Granite and Thor Lake Syenite. Diabase dykes trending northwest and east-northeast cut both Grace Lake Granite and Thor Lake Syenite. Grace Lake Granite, the largest unit of the Blatchford Lake area, underlies an area of 155 km^2 (Davidson, 1978). Thor Lake Syenite occupies a roughly oval, 30 km^2 area in the center of the Grace Lake Granite (Figure 10). Although the Thor Lake Syenite consists predominantly of amphibole-rich (ferrorichterite) syenite, with an outer border zone of fayalite-pyroxene syenite, four textural variants of the amphibole-bearing syenite are discernible in the field (Birkett et al., 1994; Trueman et al., 1984). The contacts of the Caribou Lake Gabbroon the western margin of the Blatchford Lake complex are steep, as is the outer contact of the Grace Lake Granite in most places. Although gradational over distances of one to several meters, the contact of the Thor Lake Syenite with the Grace Lake Granite at surface also appears to-be steep. Some of the observed contacts of the Caribou Lake anorthosites with the granites and syenites of the western part of the complex, on the other hand, are subhorizontal. Although they are cut in places by vertical granitic and syenitic dykes, a large part of the Caribou Lake anorthositic rocks occupy geographically higher areas and appear to be underlain by graniticand syenitic rocks (Davidson, 1978).

The objective of the airborne gravity gradiometry surveys is to measure small variations in the rate of change of the gravity field due to lateral variations in the mass and density of underlying bedrock. The survey was flown at a nominal altitude of 100 m by Falcon AGG system. Flight lines were spaced 250 m apart with a flight line direction 0f 145˚. The raw gravity data are extracted and checked by statistical analysis for performance evaluation including the use of a graphic profile display of data plots. Post-processing is done to remove the

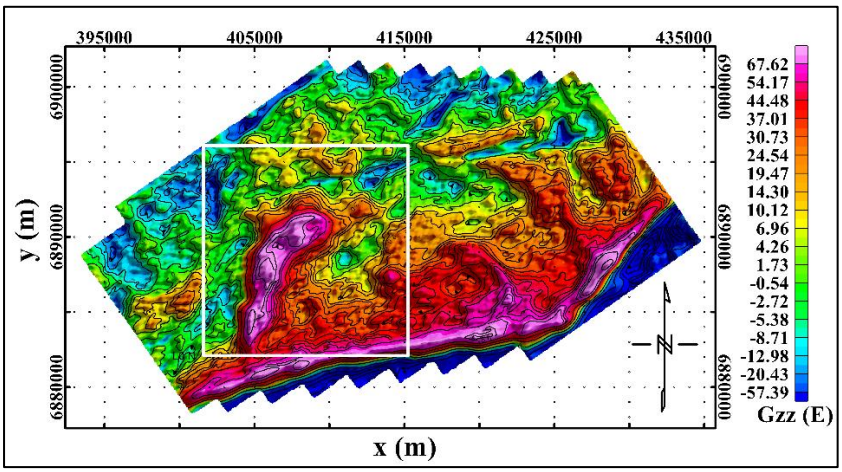

Figure 11. Gridded g_{zz} component with cell size of 50 m over Blatchford Lake. White box shows portion of grid displayed subsequent figures.

effects of aircraft acceleration by modelling the acceleration of the gradiometer environment and removing sensitivities from the output (Geological Survey of Canada, 2011).

The two corrected curvature components of the gravity tensor collected g_{xy} and g_{uv}, where $g_{uv} = (g_{xx}-g_{yy})/2$, are levelled using a least-squares minimization of differences at survey line intersections. Final transformation of the levelled data into gravity and components of the full gravity gradient tensor is accomplished using the Fourier domain transformation (Sanchez et al., 2005). The output generates all gravity tensor components. The flight surface on which the data are collected is an irregular draped surface.

To make possible the transformation of the horizontal curvature gradients g_{xy} and g_{uv} using Fourier domain potential field transfer functions requires that the data is located on a flat horizontal surface. To achieve this, the data are piece-wise upward continued to the top grazer, that is the peak elevation present in the flight surface. Following the transformation, the data are then moved back to a smoothed version of the flight surface via potential field continuation. The gradient data are demodulated and filtered along line using a 6-pole Butterworth low-pass filter with a cut-off frequency of 0.18 Hz. Terrain correction is applied to GGT data with a density of 2670 kg/m^3, based on correlation tests.

Figure 11 shows the gridded first vertical derivative of the vertical component of the gravity vector g_{zz} over the Blatchford Lake area with a cell size of 50 m. The white box is a portion of the Blatchford Lake area, which this study intends to apply the Euler's method to it. The calculated invariants I_1 and I_2 is illustrated in Figures 12a and 12b, respectively. As can be seen in these Figures, two main structures A and B enhanced. The minima of the I_1 and maxima of the I_2 are nicely located over the edges of gravity anomalies. Figures 13 and 14 shows the solutions of depth structural index from Euler deconvolution of I_1 and I_2, respectively. A starting window of 150 m×150 m is formed around the maxima of $\left|\frac{\partial I_1}{\partial z}\right|$ and $\frac{\partial I_2}{\partial z}$, and then the window size is increased until it exceeds a window size of 2 km×2 km. Solutions with an unreliable structural index, a depth to source with negative values and high uncertainty of the depth estimates normalized by corresponding depth

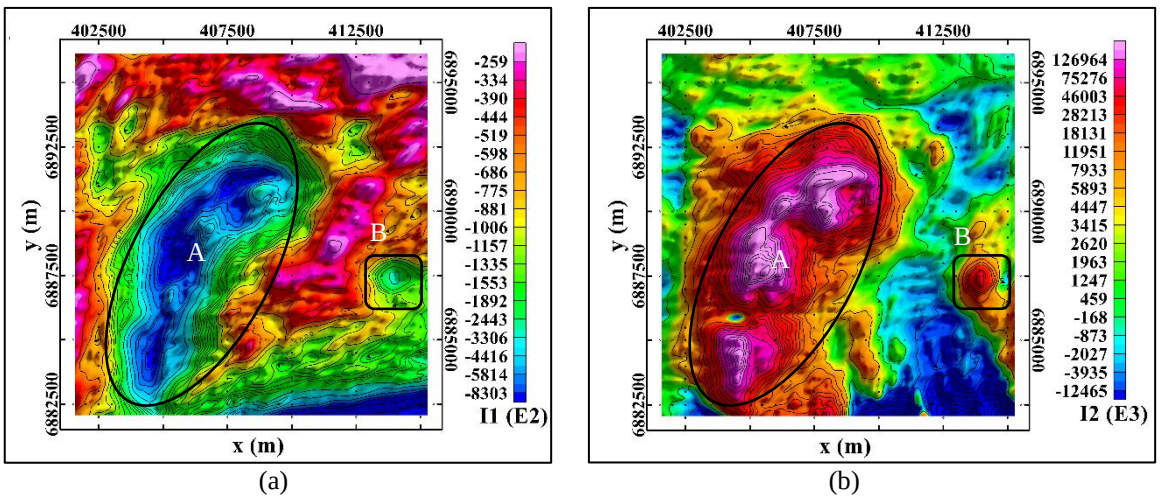

(a) (b)

Figure 12. (a) I_1 and (b) I_2 invariants calculated from measured GGT data for area in white box in Figure 10.

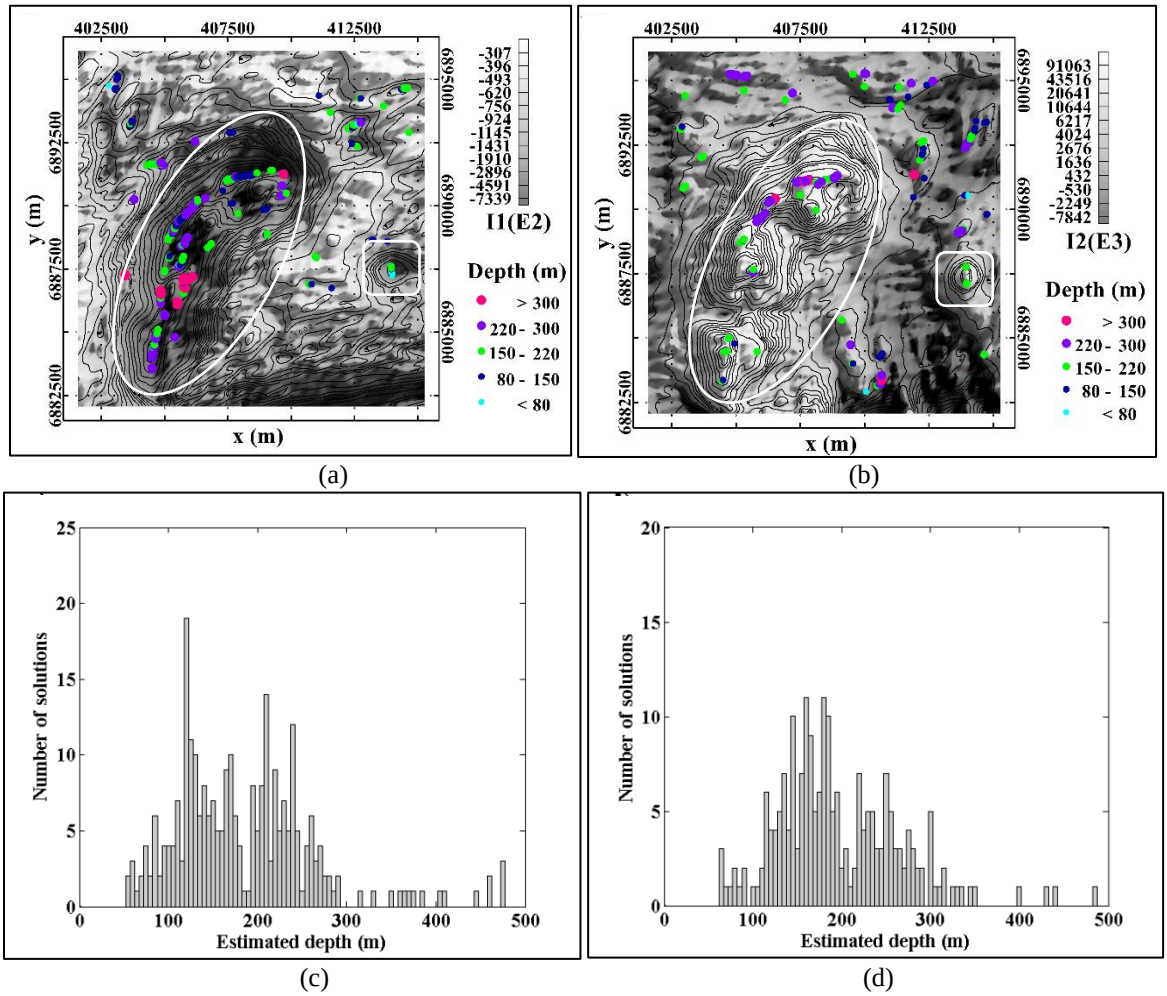

Figure 13. (a) , (b) The estimated depth from Euler deconvolution of I_1 and I_2 superimposed on corresponding maps and (c) , (d) Histogram of estimated depth from Euler deconvolution of I_1 and I_2 , respectively.

(greater than 50%) are rejected. According to Figures 12c and 12d, most estimated depths are around 150 m and 250 m. For anomaly A, I_1 shows more depth solutions than I_2, mostly in the range of 100-250 m. However, for the anomaly B, the estimated depths are in the smaller range, 150-220 m. The structural indices are mostly about (-0.8), implying that solutions are well located over the edges of gravity sources represented by geological contacts.

7 Conclusions

By using the components of the GGT simultaneously, one can calculate eigenvalues (λ_1, λ_2 and λ_3) and rotational invariants (I_1 and I_2). These parameters play an important role in the interpretation of gravity gradiometry data. It is shown that the components of the gradient tensor are homogeneous and satisfy the homogeneous Euler's equation. Using the homogeneity of these components, it is shown that the eigenvalues and invariants are also homogeneous. Therefore, they satisfy the Euler's equation, and this enables us to estimate the location and structural index of the causative sources, simultaneously. The advantage of using invariants is that it is not sensitive to orientation errors of the measurement device. Vertical derivatives of invariants have a higher resolution than themselves. Therefore, the maximum of them was applied for using in the Euler's equation. The different window sizes centered at the maximum of corresponding functions

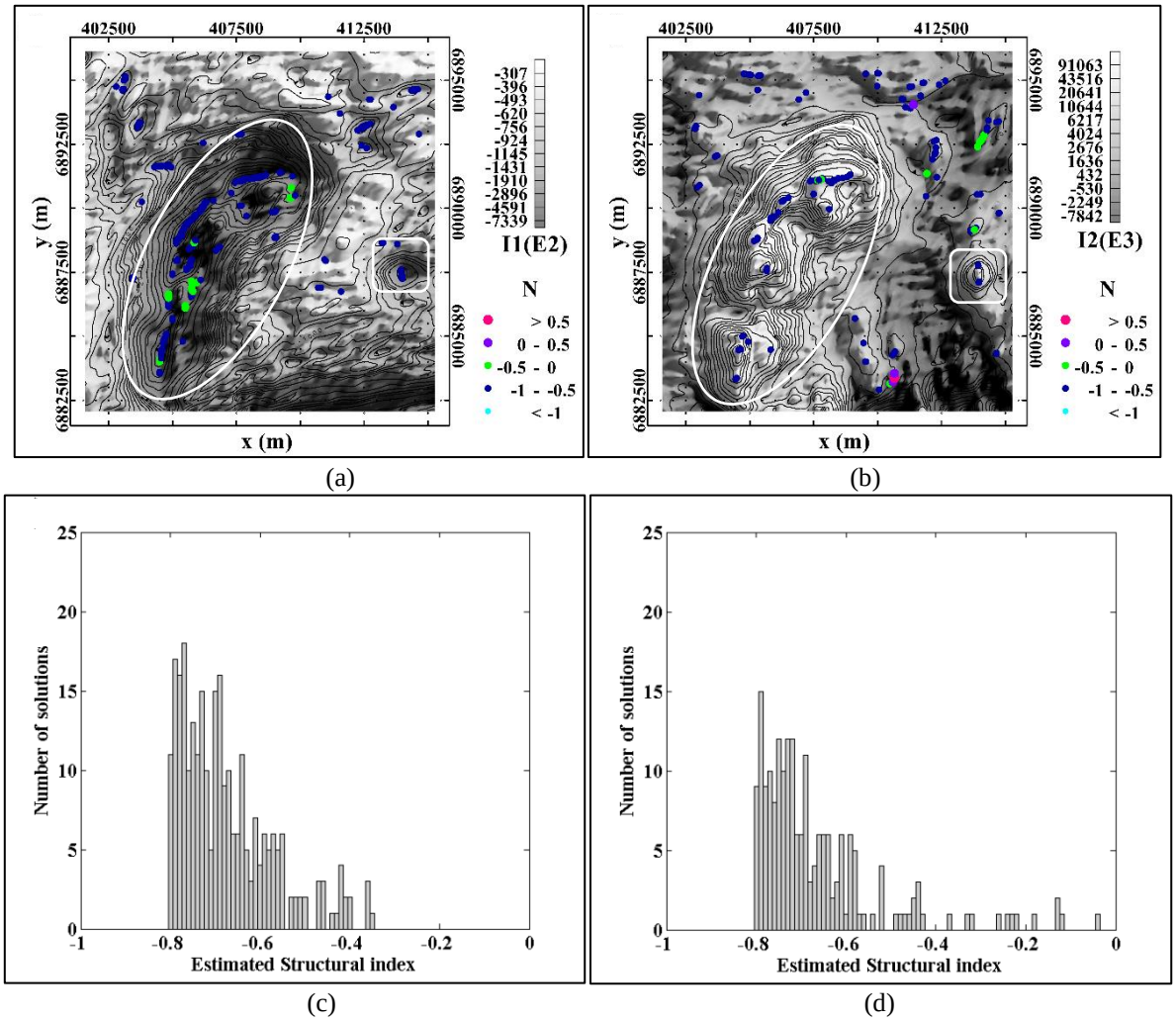

Figure 14. (a) , (b) The estimated structural index from Euler deconvolution of I_1 and I_2 superimposed on corresponding maps and (c) , (d) Histogram of estimated structural index from Euler deconvolution of I_1 and I_2, respectively.

were formed, and the Euler solution with the minimum uncertainty-to-calculated parameters were selected.

The method to noisy and without noise data was applied in the presence of interfering sources. Furthermore, using two interfering spheres, the interference errors for different separation to depths were obtained. The highest relative error was observed for the separation distance equal to the depth. Application of the Euler deconvolution of invariants on GGT data from the Blatchford Lake area shows that mainly estimated depths of gravity sources are located above the edges in range of 100-300 m, and the estimated structural indices are mainly about -0.8 corresponding well to geological contacts.

Acknowledgment

The author would like to thank Prof. Mark Pilkington and Prof. Pierre Keating for their constructive comments and suggestions that greatly improved the original version of this manuscript.

References

Beiki, M., 2010, Analytic signals of gravity gradient tensor and their application to estimate source location: Geophysics, **75**(6), I59-I74.

Beiki, M., Clark, D. A., Austin, J. R., and Foss, C. A., 2012, Estimating source location using normalized magnetic source strength calculated from magnetic gradient tensor data: Geophysics, **77**(6), J23-J37.

Beiki, M., Keating, P., and Clark, D. A., 2014, Interpretation of magnetic and gravity gradient tensor data using normalized source

strength–A case study from McFaulds Lake, Northern Ontario, Canada: Geophysical prospecting, **62**(5), 1180-1192.

Birkett, T. C., Richardson, D. G. and Sinclair, W. D., 1994, Gravity modelling of the Blatchford Lake intrusive suite, Northwest Territories: in, WD Sinclair and DG Richardson, eds, Studies of rare metal deposits in the Northwest Territories: Geological Survey of Canada, Bulletin, **475**, 5-16.

Geological Survey of Canada., 2011, Airborne geophysical surveys, gravity gradiometer and magnetic data, Blatchford Lake Area; Geological Survey of Canada, Open File 6955.

Clark, D. A., 2012, New methods for interpretation of magnetic vector and gradient tensor data I: eigenvector analysis and the normalised source strength: Exploration Geophysics, **43**(4), 267-282.

Davidson, A., 1978, The Blachford Lake intrusive suite: an Aphebian plutonic complex in the Slave Province, Northwest territories: Current Research Geological Survey of Canada Paper, **78**(1), 119-127.

Davidson, A., 1981, Petrochemistry of the Blatchford Lake complex. District of Mackenzie: Geological Survey of Canada Open File, **764**.

Davidson, A., 1982, Petrochemistry of the Blanchford Lake complex near Yellowknife, Northwest Territories.

Hoffman, P., and Kurfurst, D., 1988, Geology and tectonics. East Arm of Great Slave Lake, Northwest Territories: Geological Survey of Canada, Map A, 1628, 2.

Mikhailov, V., Pajot, G., Diament, M., and Price, A., 2007, Tensor deconvolution: A method to locate equivalent sources from full tensor gravity data: Geophysics, **72**(5), I61-I69.

Mickus, K. L. and Hinojosa, J. H., 2001, The complete gravity gradient tensor derived from the vertical component of gravity: a Fourier transform technique: Journal of Applied Geophysics, **46**(3), 159-174.

Nabighian, M. N., 1984, Toward a three-dimensional automatic interpretation of potential field data via generalized Hilbert transforms: Fundamental relations. Geophysics, **49**(6), 780-786.

Oruç, B., 2010, Depth estimation of simple causative sources from gravity gradient tensor invariants and vertical component: Pure and applied geophysics, **167**(10), 1259-1272.

Pedersen, L., and Rasmussen, T., 1990, The gradient tensor of potential field anomalies: Some implications on data collection and data processing of maps: Geophysics, **55**(12), 1558-1566.

Phillips, J. D., Hansen, R. O., and Blakely, R. J., 2007, The use of curvature in potential-field interpretation: Exploration Geophysics, **38**, 111–119.

Pilkington, M., and Beiki, M., 2013, Mitigating remanent magnetization effects in magnetic data using the normalized source strength: Geophysics, **78**(3), J25-J32.

Reid, A. B., Allsop, J., Granser, H., Millett, A. T., and Somerton, I., 1990, Magnetic interpretation in three dimensions using Euler deconvolution: Geophysics, **55**(1), 80-91.

Reid, A. B., Ebbing, J., and Webb, S. J., 2014, Avoidable Euler Errors–the use and abuse of Euler deconvolution applied to potential fields: Geophysical Prospecting, **62**(5), 1162-1168.

Roest, W. R., Verhoef, J., and Pilkington, M., 1992, Magnetic interpretation using the 3-D analytic signal: Geophysics, **57**(1), 116-125.

Sanchez, V., Sinex, D., Li, Y., Nabighian, M., Wright, D., and Smith, D. V., 2005, Processing and inversion of magnetic gradient tensor data for UXO applications: Paper presented at the Symposium on the Application of Geophysics to Engineering and Environmental Problems 2005.

Trueman, D., Pedersen, J., and Jorre, L., 1984, Geology of the Thor Lake Beryllium Deposits, An Update: Contribution to the Geology of Northwest Territories, **1**, 115-120.

Wilson, H., 1985, Analysis of the magnetic gradient tensor: Defence Research Establishment Pacific: Technical Memorandum, **8**, 5-13.

Zhang, C., Mushayandebvu, M. F., Reid, A. B., Fairhead, J. D., and Odegard, M. E., 2000, Euler deconvolution of gravity tensor gradient data: Geophysics, **65**(2), 512-520.

Zhou, W., 2016, Depth estimation method based on the ratio of gravity and full tensor gradient invariant: Pure and Applied Geophysics, **173**(2), 499-508.

Appendix A

The invariant ratio, I, is expressed by the following relation (Pedersen and Rasmussen, 1990):

$$I = -\frac{27}{4}\frac{I_2^{\,2}}{I_1^{\,3}}, \quad 0 \le I \le 1 \qquad \text{(A1)}$$

Similar to Equation (27), it can be simply shown that the homogeneity degree is zero. It is shown here in another

way that the Equation (A1) satisfies the Euler's equation. By differentiating from the Equation (A1):

$$\frac{\partial I}{\partial x}=-\frac{27}{4}\frac{2\frac{\partial I_2}{\partial x}I_2I_1-3\frac{\partial I_1}{\partial x}{I_2}^2}{{I_1}^3} \quad \text{(A2)}$$

$$\frac{\partial I}{\partial y}=-\frac{27}{4}\frac{2\frac{\partial I_2}{\partial y}I_2I_1-3\frac{\partial I_1}{\partial y}{I_2}^2}{{I_1}^3} \quad \text{(A3)}$$

$$\frac{\partial I}{\partial z}=-\frac{27}{4}\frac{2\frac{\partial I_2}{\partial z}I_2I_1-3\frac{\partial I_1}{\partial z}{I_2}^2}{{I_1}^3} \quad \text{(A4)}$$

Multiplying Equations (A2), (A3) and (A4) by $(x-x_0)$, $(y-y_0)$ and $(z-z_0)$, respectively, and using the Equations (22) and (32), it is obtained

$$(x-x_0)\frac{\partial I}{\partial x}+(y-y_0)\frac{\partial I}{\partial y}+(z-z_0)\frac{\partial I}{\partial z}= -\frac{27}{4}\left(\frac{6{I_2}^2I_1}{{I_1}^3}(N+1)-\frac{6{I_2}^2I_1}{{I_1}^3}(N+1)\right)=0 \quad \text{(A5)}$$

As can be seen, the Equation (A5) does not include the structural index (N). Therefore, using a window of data points, we can estimate the location of the causative sources.